SUBMITTED TO ApJ
Preprint typeset using LaTeX style emulateapj v. 5/2/11

EVOLUTION OF THE SIZES OF GALAXIES OVER $7 < z < 12$ REVEALED BY THE 2012 HUBBLE ULTRA DEEP FIELD CAMPAIGN

Yoshiaki Ono[1], Masami Ouchi[1,2], Emma Curtis-Lake[3], Matthew A. Schenker[4], Richard S. Ellis[4], Ross J. McLure[3], James S. Dunlop[3], Brant E. Robertson[5], Anton M. Koekemoer[6], Rebecca A.A. Bowler[3], Alexander B. Rogers[3], Evan Schneider[5], Stephane Charlot[7], Daniel P. Stark[5], Kazuhiro Shimasaku[8], Steven R. Furlanetto[9], Michele Cirasuolo[3,10]

submitted to ApJ

ABSTRACT

We analyze the redshift- and luminosity-dependent sizes of dropout galaxy candidates in the redshift range $z \sim 7-12$ using deep images from the 2012 Hubble Ultra Deep Field (UDF12) campaign, data which offers two distinct advantages over that used in earlier work. Firstly, we utilize the increased signal-to-noise ratio offered by the UDF12 imaging to provide improved size measurements for known galaxies at $z \simeq 6.5-8$ in the HUDF. Specifically, we stack the new deep F140W image with the existing F125W data in order to provide improved measurements of the half-light radii of z'-band dropouts (at $z \simeq 7$). Similarly we stack this image with the new deep UDF12 F160W image to obtain new size measurements for a sample of Y-band dropouts (at $z \simeq 8$). Secondly, because the UDF12 data have allowed the construction of the first robust galaxy sample in the HUDF at $z > 8$, we have been able to extend the measurement of average galaxy size out to significantly higher redshifts. Restricting our size measurements to sources which are now detected at $> 15\sigma$, we confirm earlier indications that the average half-light radii of $z \sim 7-12$ galaxies are extremely small, $0.3-0.4$ kpc, comparable to the sizes of giant molecular associations in local star-forming galaxies. We also confirm that there is a clear trend of decreasing half-light radius with increasing redshift, and provide the first evidence that this trend continues beyond $z \simeq 8$. Modeling the evolution of the average half-light radius as a power-law, $\propto (1+z)^s$, we obtain a best-fit index of $s = -1.28 \pm 0.13$ over the redshift range $z \sim 4-12$, mid-way between the physically expected evolution for baryons embedded in dark halos of constant mass ($s = -1$) and constant velocity ($s = -1.5$). A clear size-luminosity relation, such as that found at lower redshift, is also evident in both our z- and Y-dropout sample. This relation can be interpreted in terms of a constant surface density of star formation over a range in luminosity of $0.05-1.0L^*_{z=3}$. Our results also strengthen previous claims that the star-formation surface density in dropout galaxies is broadly unchanged from $z \simeq 4$ to $z \simeq 8$ at $\Sigma_{\rm SFR} \simeq 2\,{\rm M_\odot\,yr^{-1}\,kpc^{-2}}$. This value is $2-3$ orders of magnitude lower than that found in extreme starburst galaxies, but is very comparable to that seen today in the centers of normal disk galaxies. This provides further support for a steady smooth build-up of the stellar populations in galaxies in the young universe.

Subject headings: galaxies: formation — galaxies: evolution — galaxies: high-redshift — galaxies: structure

1. INTRODUCTION

Considerable progress has been made in charting the abundance of galaxies at $z \sim 7-10$ from deep imaging with ground-based observations and various campaigns undertaken with the Wide Field Camera 3 infrared channel (WFC3/IR) on *Hubble Space Telescope* (HST). Sample selection makes use of the well-established dropout technique, which takes advantage of the unique spectral characteristics of high-redshift star-forming galaxies, i.e., a blue UV spectrum and a sharp drop in flux at wavelengths shorter than Lyα. These complementary studies have identified a large number of dropout galaxies at $z \sim 7$ and beyond. Investigating the abundance of dropout galaxies over $7 < z < 10$ has revealed a clear decrease in the number density of luminous galaxies with increasing redshift (e.g., Ouchi et al. 2009; McLure et al. 2010; Castellano et al. 2010; Oesch et al. 2010b; Bouwens et al. 2011b).

Characterizing the evolution of galaxy morphologies and sizes is useful for understanding galaxy formation history. Analytical studies have calculated the size-redshift relation of disk galaxies, suggesting the typical size of galaxies of a given luminosity is expected to decrease with increasing redshift (Mo et al. 1998, 1999). The virial radius of a dark matter halo scales with redshift and virial velocity or virial mass. Assuming that the

ono@icrr.u-tokyo.ac.jp
[1] Institute for Cosmic Ray Research, The University of Tokyo, Kashiwa 277-8582, Japan
[2] Kavli Institute for the Physics andMathematics of the Universe (Kavli IPMU), WPI, The University of Tokyo, Chiba 277-8583, Japan
[3] Institute for Astronomy, University of Edinburgh, Royal Observatory, Edinburgh EH9 3HJ, UK
[4] Department of Astrophysics, California Institute of Technology, MS 249-17, Pasadena, CA 91125
[5] Department of Astronomy and Steward Observatory, University of Arizona, Tucson AZ 85721
[6] Space Telescope Science Institute, Baltimore, MD 21218
[7] UPMC-CNRS, UMR7095, Institut dfAstrophysique, F-75014 Paris, France
[8] Department of Astronomy, Graduate School of Science, The University of Tokyo, Tokyo 113-0033, Japan
[9] Department of Physics & Astronomy, University of California, Los Angeles CA 90095
[10] UK Astronomy Technology Centre, Royal Observatory, Edinburgh EH9 3HJ, UK

exponential scale length of the baryonic disc scales with the virial radius, the sizes of disks are expected to scale with redshift, proportional to $H(z)^{-1}$ at a fixed mass or $H(z)^{-2/3}$ at a fixed circular velocity (e.g., Ferguson et al. 2004), where $H(z)$ is the Hubble parameter which scales as $\sim (1+z)^{3/2}$ at high redshifts.

Earlier observations have reported that the sizes (half-light radii) of dropout galaxies decrease according to about $(1+z)^{-1}$ up to $z \sim 7$ (Oesch et al. 2010a), which is expected at fixed halo masses, and in good agreement with previous estimates at lower redshifts (Bouwens et al. 2004). However, because they used only the first epoch of their survey data with the WFC3/IR, their analysis still shows large uncertainties, especially in their fainter sample. Therefore, it is also consistent with $(1+z)^{-1.5}$ (Ferguson et al. 2004; Hathi et al. 2008), as expected for sizes that scale with halo circular velocity.

Oesch et al. (2010a) have also reported that the star-formation rate (SFR) surface densities of dropout galaxies remains constant from $z \sim 7$ to $z \sim 4$. They suggest a possible explanation is that the average star formation efficiency is very similar in all these galaxies, and that feedback effects change the mode of star formation by only a small amount. It would be interesting to see if this possible trend continues toward higher redshifts, to infer star-formation activities in galaxies at earlier epochs of galaxy formation.

Recently, a new campaign was carried out with the WFC3/IR to significantly deepen the Hubble Ultra Deep Field in 2012 (GO 12498; PI: R. Ellis, hereafter UDF12: Ellis et al. 2012 and Koekemoer et al. 2012 for the project description); this yields the deepest near-infrared images ever obtained. Additional scientific results from this project are presented in Dunlop et al. (2012), Schenker et al. (2012), McLure et al. (2012), and Robertson et al. (2012). In this paper, we study morphologies of $z \sim 7-12$ galaxies based on the complete WFC3/IR UDF12 data set. The advantages of the new images are (i) a new F140W image and a deeper F160W data from which we obtain robust estimates on the rest-frame UV morphologies of galaxies not only at $z \sim 7$, but also $z \sim 8-12$ for the first time, (ii) a deeper F105W image which enables us to safely exclude contaminations by foreground sources from our galaxy samples at $z \sim 8$ and beyond[11]. The purpose of this paper is to investigate the galaxy size and SFR surface density evolution beyond $z \sim 7$, and the correlation of size with UV luminosity.

The outline of this paper is as follows. After describing the imaging data used in this study in Section 2, we summarize our dropout galaxy samples in Section 3. Our size analysis is described in Section 4. In Section 5, we investigate the size-luminosity relation and the size evolution and discuss the implications. A summary is given in Section 6. Throughout this paper, we use magnitudes in the AB system (Oke & Gunn 1983) and assume a flat universe with $(\Omega_{\rm m}, \Omega_\Lambda, h) = (0.3, 0.7, 0.7)$. In this cosmological model, an angular dimension of 1.0 arcsec corresponds to a physical dimension of 5.365 kpc arcsec^{-1} at $z = 6.7$, 4.818 kpc arcsec^{-1} at $z = 8.0$, 4.465 kpc arcsec^{-1} at $z = 9.0$, and 3.683 kpc arcsec^{-1} at $z = 11.9$. We express galaxy UV luminosities in units of the characteristic luminosity of $z \sim 3$ galaxies, $L^*_{z=3}$, which corresponds to $M_{1600} = -21.0$ (Steidel et al. 1999). The four WFC3/IR filters we use, F105W, F125W, F140W and F160W are denoted by Y_{105}, J_{125}, J_{140} and H_{160}, respectively. We also use four ACS filters, F435W, F606W, F775W and F850LP, which are denoted by B_{435}, V_{606}, i_{775} and z_{850}, respectively.

[11] We do not use our deep F105W image for the morphology analysis of $z \sim 7$ galaxies, since a redshifted Lyα and the continuum break of an object at $z \gtrsim 6.4$ enters the F105W band.

2. OBSERVATIONS

The primary data set used in this morphology analysis for $z \sim 7-12$ galaxies is the ultra-deep WFC3/IR observations taken for the UDF12 campaign combined with images taken for the UDF09 campaign (GO 11563; PI: G. Illingworth). In the UDF09 campaign, WFC3/IR data was obtained over three fields: the HUDF main, and two parallel fields. The UDF12 campaign has obtained 128 orbits of WFC3/IR data over the HUDF main field. We have combined all the exposures including the data from other HST programs (GO12060, 12061, 12062; PI: S. Faber, H. Ferguson; GO12099; PI: A. Riess). In total, the observations over the HUDF main field include 253 orbits (F105W: 100 orbits, F125W: 39 orbits, F140W: 30 orbits, F160W: 84 orbits). A more detailed description of the UDF12 data set is provided by Koekemoer et al. (2012), and the final reduced data are being made publicly available as High-Level Science Products[12] that are delivered to the Space Telescope Science Institute archive, and further details and current updates about the survey are provided at the project website[13].

To minimize the effects of morphological K-correction and take the advantage of the UDF12 campaign, we measure sizes of galaxies in the images of the WFC3/IR band that is the closest to the rest-frame $1600-1700$Å. A stack of the PSF-matched J_{125}- and J_{140}-band images is used for z_{850}-dropouts, a stack of the PSF-matched J_{140}- and H_{160}-band images for Y_{105}-dropouts, and the H_{160}-band image for candidates at $z > 8.5$. Their 5σ limiting magnitudes are 29.8 ($J_{125}+J_{140}$), 29.7 ($J_{140}+H_{160}$), and 29.5 (H_{160}) within filter-matched apertures, which are $0.45-0.50$ arcsec in diameter (Ellis et al. 2012). We use images with a pixel scale of 0.03 arcsec pixel^{-1}.

3. SAMPLES

We investigate the sizes of $z \sim 7-12$ galaxies based on the the $z \sim 7-8$ samples selected by Schenker et al. (2012) and the $z > 8.5$ samples whose photometric redshifts from SED fitting analysis are available in McLure et al. (2012) (see also Ellis et al. 2012). Here we briefly summarize how these galaxies are selected.

To select star-forming galaxies at $z \sim 7-8$, Schenker et al. (2012) applied the dropout technique, which probes a blue UV spectrum and a spectral break blueward of Lyα due to IGM absorption. For $z \sim 7$ z_{850}-dropout galaxies, they first required a 3.5σ detection in Y_{105} plus one of the other filters which probe longer wavelengths (J_{125}, J_{140}, or H_{160}). Then they applied the two color criteria: $z_{850} - Y_{105} > 0.7$ and $Y_{105} - J_{125} < 0.4$. Also the following criteria were used; (i) the significance

[12] http://archive.stsci.edu/prepds/hudf12/
[13] http://udf12.arizona.edu/

Table 1
Bright z_{850}- and Y_{105}-Dropout Galaxies in the HUDF Reported in the Literature

ID	(1)	(2)	(3)	(4)	(5)	(6)	(7)	(8)	(9)	(10)
Bright z_{850}-dropouts										
UDF12-4258-6567	UDF-640-1417	—	UDFz-42566566	688	1441	A032	zD1	HUDF.z.4444	UDFz-42566566	HUDF-658
UDF12-3746-6327	—	—	—	837	769	—	—	—	—	HUDF-796
UDF12-4256-7314	UDF-387-1125	—	UDFz-42577314	1144	2432	A008	zD3	HUDF.z.6433	UDFz-42567314	—
UDF12-4219-6278	—	—	—	1464	649	—	—	HUDF.z.2677	UDFz-42196278	HUDF-1442
UDF12-3677-7535	—	—	UDFz-36777536	1911	2894	—	—	HUDF.z.7462	UDFz-36777536	HUDF-1473
UDF12-4105-7155	—	—	UDFz-41057156	2066	2013	A017	—	—	—	—
UDF12-3958-6564	—	—	UDFz-39586565	1915	1445	A033	—	—	UDFz-39576564	HUDF-1995
UDF12-3744-6512	—	—	UDFz-37446513	1880	1289	A040	—	HUDF.z.4121	UDFz-37446512	HUDF-1632
UDF12-3638-7162	—	—	UDFz-36387163	1958	2032	A016	zD6	HUDF.z.5659	UDFz-36377163	HUDF-1818
Bright Y_{105}-dropouts										
UDF12-3879-7071	UDF-983-964	HUDF-480	UDFz-38807073	835	1768	A025	zD2	HUDF.z.5141	UDFy-38807071	HUDF-860
UDF12-4470-6442	—	—	UDFz-44716442	1107	1106	A044	zD7	—	UDFy-44706443	HUDF-1173
UDF12-3952-7173	—	—	—[†1]	1422	2055	B041	—[†2]	—	UDFy-39537174	—
UDF12-4314-6284	—	—	UDFz-43146285	1678	669	A060	zD5	HUDF.z.2714	UDFy-43136284	HUDF-1419
UDF12-3722-8061	—	—	UDFz-37228061	1574	3053	A003	zD9	—	UDFy-37218061	HUDF-1660
UDF12-3813-5540	—	—	UDFy-38135539	1721	125	B115	YD3	HUDF.YD3	UDFy-38125539	HUDF-2003
Bright $z > 8.5$ candidates										
UDF12-3954-6284	—	—	—	—	—	—	—	—	UDFj-39546284	—

Note. — (1) Bouwens et al. (2008) ; (2) Oesch et al. (2009); (3) Oesch et al. (2010b) and Bouwens et al. (2010); (4) McLure et al. (2010); (5) Finkelstein et al. (2010); (6) Yan et al. (2010); (7) Bunker et al. (2010); (8) Wilkins et al. (2011) and Lorenzoni et al. (2011); (9) Bouwens et al. (2011b) and Bouwens et al. (2011a); (10) McLure et al. (2011). UDF12-4258-6567 has been spectroscopically confirmed by Fontana et al. (2010).

[†1] Close to UDFz-39557176.
[†2] Close to zD4.

Table 2
Photometric Redshifts for Bright z_{850}- and Y_{105}-Dropout Galaxies Found in the HUDF

ID	ID(i)	$z_{\rm photo}$	$\delta z_{\rm photo}$	ID(ii)	$z_{\rm photo}$	$\delta z_{\rm photo}$	ID(iii)	$z_{\rm photo}$
Bright z_{850}-dropouts								
UDF12-4258-6567	688	6.70	(6.50-6.90)	1441	6.83	(6.70-6.98)	40250	7.05
UDF12-3746-6327	837	6.35	(6.15-6.55)	769	6.36	(6.09-6.47)	—[†1]	—[†1]
UDF12-4256-7314	1144	6.80	(6.50-7.10)	2432	6.86	(6.70-7.01)	40332	7.20
UDF12-4219-6278	1464	6.30	(5.95-6.75)	649	6.40	(6.25-6.58)	20075	6.70
UDF12-3677-7535	1911	6.40	(6.20-6.60)	2894	6.34	(6.21-6.49)	40396	6.50
UDF12-4105-7155	2066	7.20	(6.50-7.80)	2013	6.70	(6.48-7.03)	40296	7.05
UDF12-3958-6564	1915	6.40	(6.15-6.65)	1445	6.40	(6.17-6.61)	40252	6.80
UDF12-3744-6512	1880	6.50	(6.25-6.80)	1289	6.38	(6.22-6.55)	40226	6.70
UDF12-3638-7162	1958	6.50	(6.25-6.80)	2032	6.40	(6.23-6.58)	40309	6.55
Bright Y_{105}-dropouts								
UDF12-3879-7071	835	7.20	(6.90-7.50)	1768	7.22	(7.08-7.40)	40278	7.65
UDF12-4470-6442	1107	7.60	(7.30-7.90)	1106	7.32	(7.12-7.53)	40197	7.70
UDF12-3952-7173	1422	7.60	(7.00-8.05)	2055	7.81	(7.48-8.24)	70284	7.85
UDF12-4314-6284	1678	7.05	(6.60-7.40)	669	7.25	(7.00-7.57)	40143	7.30
UDF12-3722-8061	1574	7.20	(6.55-7.60)	3053	7.40	(7.12-7.70)	40410	7.70
UDF12-3813-5540	1721	8.45	(7.75-8.85)	125	8.61	(8.19-8.89)	70020	8.30

Note. — (i) McLure et al. (2010); (ii) Finkelstein et al. (2010); (iii) McLure et al. (2012). $\delta z_{\rm photo}$ denotes 1σ confidence interval.

[†1] This object is not included in the catalog of McLure et al. (2012), because its photometric redshift is less than 6.5.

is less than 2.0σ in B_{435}, V_{606}, and i_{775}; (ii) the significance is not more than 1.5σ in more than one band among B_{435}, V_{606}, and i_{775}; (iii) $\chi^2_{\rm opt} < 5.0$ [14]. For $z \sim 8$ Y_{105}-dropout galaxies, they required a 3.5σ detection in J_{125} and one of the other filters which probe longer wavelengths, J_{140} and H_{160}. From the detected objects, they selected dropouts which satisfy the two color criteria, $Y_{105} - J_{125} > 0.5$ and $J_{125} - H_{160} < 0.4$, and the following criteria for the optical data; (i) the significance is less than 2.0σ in B_{435}, V_{606}, i_{775}, and z_{850}; (ii) the significance is not more than 1.5σ in more than one band among B_{435}, V_{606}, i_{775}, and z_{850}; (iii) $\chi^2_{\rm opt} < 5.0$. By using these selection criteria, Schenker et al. (2012) identified 47 z_{850}-dropouts and 27 Y_{105}-dropouts in the HUDF main field. McLure et al. (2012) independently searched for galaxies at $z \gtrsim 7$ using the photometric redshift technique. The objects in their catalog with photometric redshifts $z_{\rm photo} \sim 7-9$ are well matched with the objects in the z_{850}- and Y_{105}-dropout catalogs constructed by Schenker et al. (2012).

In addition to the dropout galaxies, we study $z > 8.5$ star-forming galaxy candidates reported by Ellis et al. (2012). They located all sources by examining the stack of the final J_{125}-, J_{140}-, and H_{160}-band images and applied the photometric redshift technique (see also, McLure et al. 2012), making use of the full data set obtained by the UDF12 program and the previous programs. They also applied the dropout technique for the master catalog, searching for objects undetected at 2σ in both Y_{105} (> 31.0 mag) and in a combined ACS image. By both of the two techniques, they have found seven convincing $z > 8.5$ candidates.

Morphology measurements for galaxies require a signif-

[14] $\chi^2_{\rm opt}$ is defined by $\chi^2_{\rm opt} = \Sigma_i {\rm SGN}(f_i)\,(f_i/\sigma_i)^2$ where f_i is the flux in band i, σ_i is the uncertainty of f_i, and ${\rm SGN}(f_i)$ is 1 if $f_i > 0$ and -1 if $f_i < 0$, considering the bands shorter than Lyα (Bouwens et al. 2011b). For z_{850}-dropouts, B_{435}, V_{606}, and i_{775} are considered, and for Y_{105}-dropouts, B_{435}, V_{606}, i_{775}, z_{850} are considered.

icant detection in not only the central region of sources, but also the outer structures. Recently, Mosleh et al. (2012) reported that, in order to recover the input sizes of their realistic simulations, a signal-to-noise (S/N) ratio of at least 10 is required. To obtain robust estimates on galaxy morphologies, we set a more strict criterion for S/N; we analyze our dropouts individually down to S/N of 15. The number of z_{850}-dropouts and Y_{105}-dropouts with detection greater than 15σ in $J_{125}+J_{140}$ and $J_{140}+H_{160}$ (about 28.5 mag in the filter-matched apertures) is 9 and 6, respectively.

In order to extend our analysis to fainter magnitudes, we divide the samples into three luminosity bins, $L = (0.3-1)L^*_{z=3}$, $L = (0.12-0.3)L^*_{z=3}$, $L = (0.048-0.12)L^*_{z=3}$, based on their total magnitudes in $J_{125}+J_{140}$ for z_{850}-dropouts and $J_{140}+H_{160}$ for Y_{105}-dropouts. Since it is difficult to establish reliable total magnitudes for faint sources (S/N < 15) using `GALFIT`, we subdivide the galaxies into luminosity bins based on aperture magnitudes which contain 70% of a point-source flux, after making the appropriate aperture correction to 100% of anticipated point-source flux (McLure et al. 2012). We make median-stacked images separately for the second and third brightest luminosity bins. The number of z_{850}-dropouts (Y_{105}-dropouts) with $L = (0.12-0.3)L^*_{z=3}$ is 8 (7), while the number with $L = (0.048-0.12)L^*_{z=3}$ is 17 (13). Note that, among the 8 z_{850}-dropouts (the 7 Y_{105}-dropouts) in the second brightest luminosity bin, 7 (3) are individually detected at more than 15σ in $J_{125}+J_{140}$ ($J_{140}+H_{160}$). We do not use stacked images for the objects in the brightest luminosity bin, since the numbers of the objects are small. We also tried stacking objects fainter than $L = 0.048L^*_{z=3}$, but they did not provide meaningful size constraints.

Within the $z > 8.5$ sample, UDF12-3954-6284 has a relatively high photometric redshift, $z_{\rm photo} = 11.9$, while the others have $z_{\rm photo} = 8.6-9.5$ (Ellis et al. 2012; McLure et al. 2012). Thus, we divide them into two subsamples: one with UDF12-3954-6284 and the other with the remaining six objects. The average photometric redshift of the latter subsample is about 9.0. Since most of these objects are quite faint, we make a stack of the H_{160} images of the six $z \simeq 9$ objects, giving a detection with S/N ~ 9.

Note that the nature of the $z \sim 12$ source is still uncertain, because of its accompanying diffuse morphology (Section 4.2) and its luminosity, particularly given the lack of other detections beyond $z \sim 10.5$ (Ellis et al. 2012). Nevertheless, since no alternative, plausible explanation for this object has yet been proposed, we analyze this object as a $z \sim 12$ candidate individually.

In our following analysis, we treat the 9 z_{850}-dropouts and 6 Y_{105}-dropouts with $> 15\sigma$ detections individually, and also the 4 stacked objects at $z \sim 7-8$. In addition, we analyze the stacked $z \simeq 9$ object and the $z = 11.9$ object.

Note that our bright dropouts have been found in the literature as summarized in Table 1. Table 2 summarizes their photometric redshifts reported so far.

4. SIZES OF GALAXIES AT $z \sim 7-12$

The Sérsic power law (Sersic 1968) is one of the most frequently used profiles to study galaxy morphology and has the following form:

$$\Sigma(r) = \Sigma_e \exp\left(-b_n\left[\left(\frac{r}{r_e}\right)^{1/n} - 1\right]\right), \quad (1)$$

where Σ_e is the surface brightness at the half-light radius r_e, n is the Sérsic index, which is often referred to as the concentration parameter; larger n values denote steeper inner profiles and highly extended outer wings. The parameter r_e is the half-light radius, which holds half of the total flux inside. To make this definition true, the variable b_n depends on n. We fit the two-dimensional surface brightness profile using the `GALFIT` software version 3 (Peng et al. 2002, 2010), which convolves a galaxy model profile image with a PSF profile and optimizes the fits using Levenberg-Marquardt algorithm for χ^2 minimization. The output parameters include the centroid coordinates of the objects, their total magnitude, half-light radius, Sérsic index n, axis ratio, and position angle. The half-light radius provided by `GALFIT` is the radius along the semi-major axis, a. For each galaxy, we calculate the circularized half-light radius, $r_e = a\sqrt{b/a}$, where b/a is the axis ratio. The initial parameters used for profile fitting are provided by `SExtractor` (Bertin & Arnouts 1996), and all of the parameters, except for the Sérsic index, n, are allowed to vary during the fitting procedure. The Sérsic index n is fixed at 1.0, which corresponds to the exponential profile[15]. In this case, $b_n = 1.678$, which is obtained by solving the following equation: $\gamma(2n, b_n) = \Gamma(2n)/2$, where γ is the incomplete gamma function, and Γ is the gamma function. Noise images, required to weight individual pixels in the fit, are taken to be the root mean square (rms) maps generated from variance maps provided by the data reduction. We also use segmentation images which are produced by `SExtractor`, to mask objects other than the object we are interested in during the profile fitting.

4.1. *Simulations of Systematic Effects*

Low surface brightness in the outskirts of a galaxy may not be correctly measured by `GALFIT`, leading to systematically low measured half-light radii and/or total magnitudes. In order to quantify and correct for any such systematic effects, we use the following simulations.

First, we produce galaxy images whose Sérsic index n is fixed at 1.0, half-light radius r_e is randomly chosen between 0.5 and 10.5 pixels, and total magnitude is randomly chosen between 26 and 30 mag. Note that axis ratios are fixed at 1 during the simulations. This means that the systematic and statistical uncertainties will be larger than those obtained by our simulations, if output axis ratio is smaller than 1[16]. Then we convolve them with a PSF image which is a composite of bright and unsaturated stellar objects in the HUDF (Pirzkal et al. 2005). Figure 1 shows the measured PSFs for the $J_{125}+J_{140}$, $J_{140}+H_{160}$, and H_{160} images. The

[15] Although Oesch et al. (2010a) set the Sérsic index n to be 1.5 during their analysis, we confirm that measured sizes show very little difference if we use $n = 1.5$.

[16] If axis ratios are parametrized, measurements of circularized radii are systematically underestimated by about 10 % and the statistical uncertainties in the measured circularized radii are about 40 % at S/N = 15 (Yuma et al. 2012 in preparation).

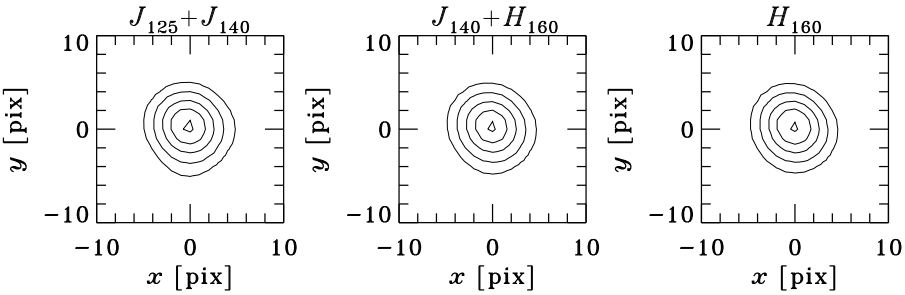

Figure 1. The contours of PSF images in $J_{125}+J_{140}$ (left), $J_{140}+H_{160}$ (middle), and H_{160} (right). The half-light radii of the PSFs are 0.119 arcsec (3.97 pixels) in $J_{125}+J_{140}$, 0.124 arcsec (4.14 pixels) in $J_{140}+H_{160}$. and 0.123 arcsec (4.12 pixels) in H_{160}.

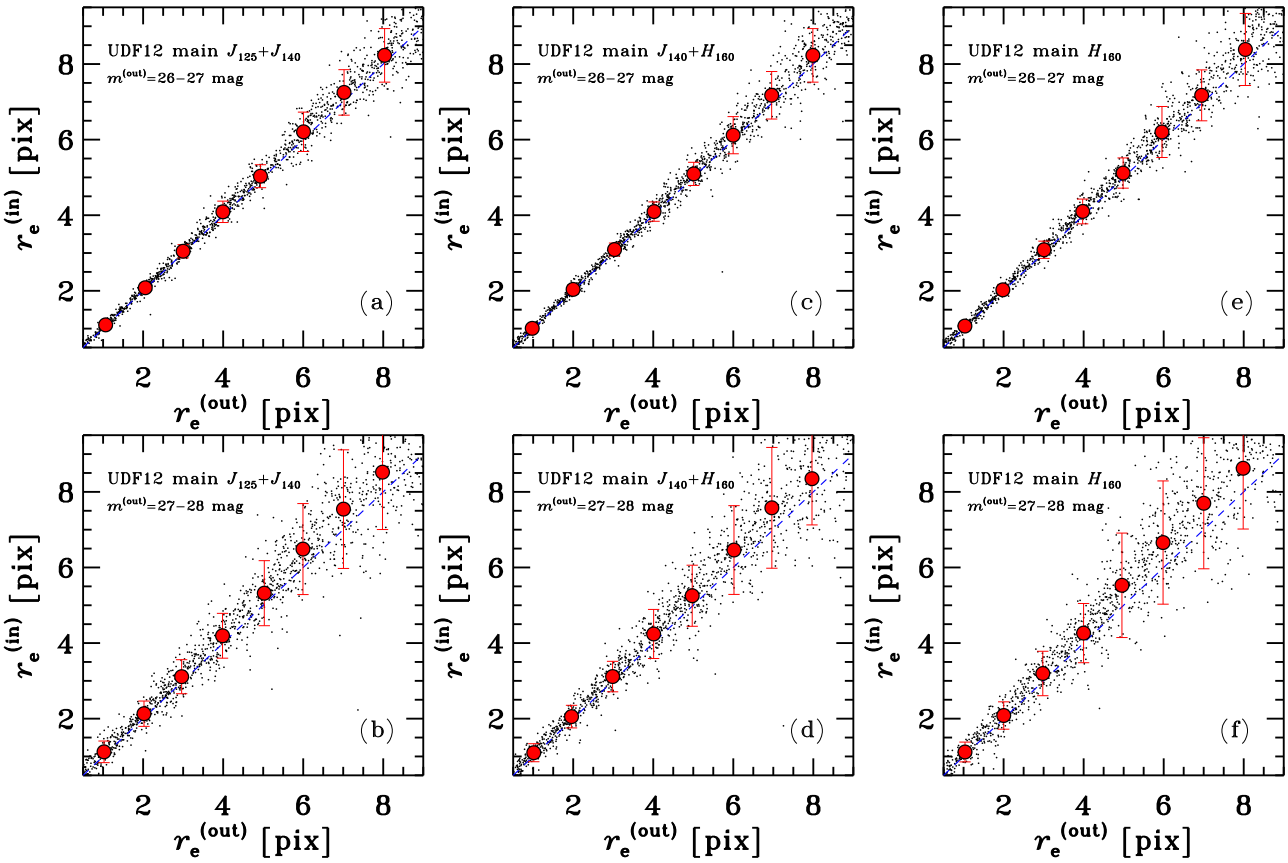

Figure 2. Panels (a)−(b), (c)−(d), and (e)−(f) show the results of our simulations for z_{850}-dropouts, Y_{105}-dropouts and $z > 8.5$ candidates, respectively. These figures show input half-light radius $r_e^{(\rm in)}$ versus output radius $r_e^{(\rm out)}$ for a range of output magnitudes, $m^{(\rm out)} = 26-27$ (a, c, e) and $27-28$ mag (b, d, f). The red filled circles and the red error bars denote the average value and the relevant rms. The blue dashed line shows the relation of $r_e^{(\rm in)} = r_e^{(\rm out)}$.

PSF-convolved galaxy images are inserted into empty regions of the original images before being analyzed in an identical manner to the true galaxy sample.

Figure 2 displays the results of size measurements of our simulated galaxies. The panels show $r_e^{(\rm in)}$ vs. $r_e^{(\rm out)}$ for each image at two different magnitude ranges ($26 < m^{(\rm out)} < 27$ and $27 < m^{(\rm out)} < 28$). We see that measurements for all images give low systematic offsets for objects with sizes smaller than ~ 4 pixels, although at larger sizes the profiles are progressively underestimated as the surface brightness of the objects decrease. The systematics are also seen to be larger for the fainter objects. We also use these simulation results for estimating statistical errors in the measurements.

Figure 3 shows the results for measured total magnitudes compared to input magnitude. This time the results are displayed in two size bins ($1 < r_e^{(\rm out)} < 3$ pixels, $3 < r_e^{(\rm out)} < 5$ pixels) for each image. The results for the smaller size bin show that the total measured magnitude is robust down to ~ 28 mag. For objects fainter than this the measured magnitude is systematically fainter than the intrinsic value, and the statistical errors increase. The trend is similar for both size bins but the results for larger objects show greater systematic offsets and statistical uncertainties.

In summary, our simulations show that GALFIT mea-

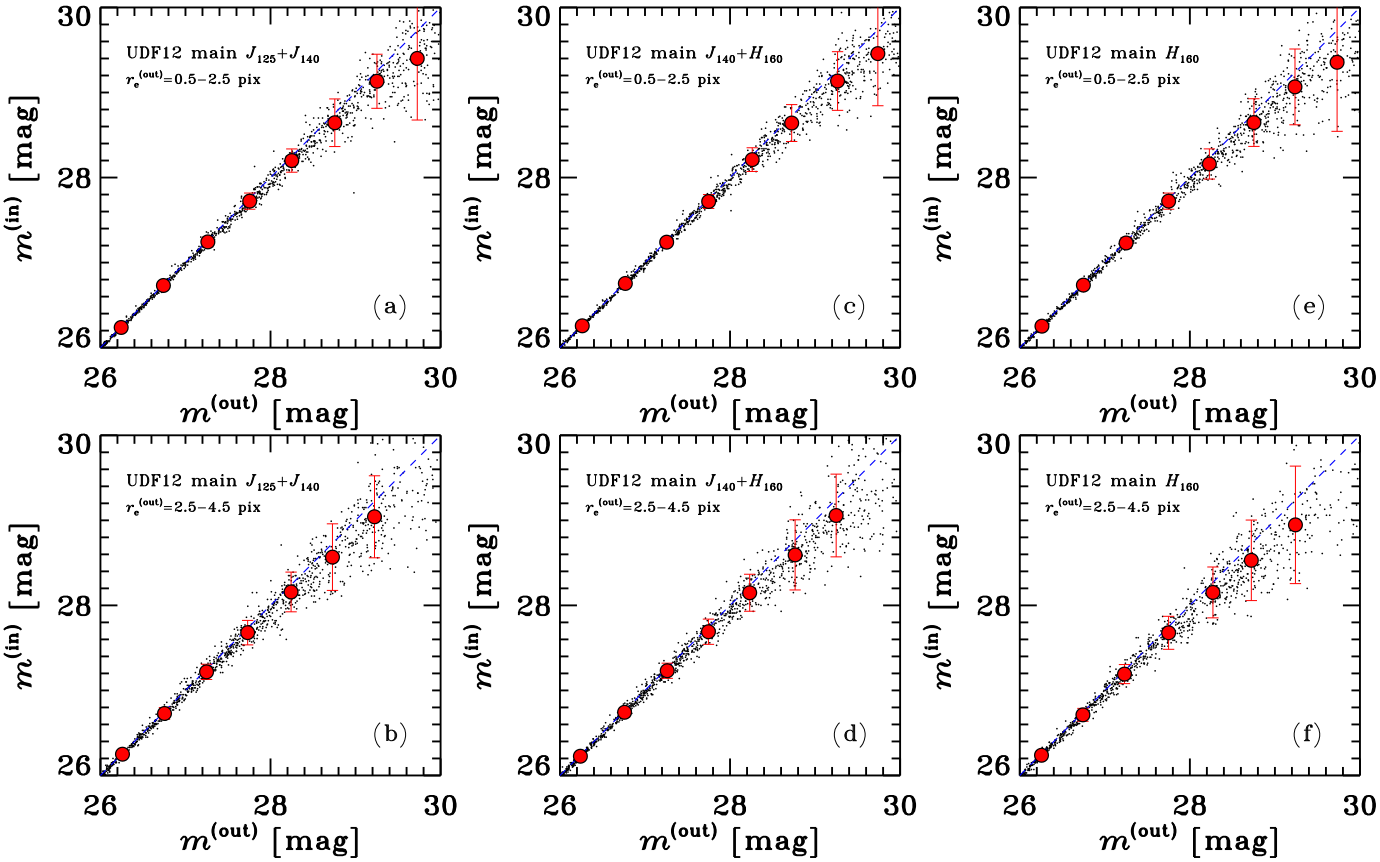

Figure 3. Panels (a)−(b), (c)−(d), (e)−(f) show the results of our simulations for z_{850}-dropouts, Y_{105}-dropouts, and $z > 8.5$ candidates, respectively. These figures show input magnitude $m^{(\rm in)}$ versus output magnitude $m^{(\rm out)}$ for a range of output half-light radii, $r_e^{(\rm out)} = 1-3$ (a, c, e) and $3-5$ pixels (b, d, f). The red filled circles and the red error bars denote the average value and the relevant rms. The blue dashed line shows the relation of $m^{(\rm in)} = m^{(\rm out)}$.

surements of half-light radii and total magnitudes are systematically underestimated for faint objects. We correct for systematic effects in the half-light radii and total magnitudes using the measured offsets in Figures 2 and 3, respectively. Note that the errors on r_e and total magnitude reported in this paper are also taken from these simulations.

4.2. *GALFIT Measurements*

We perform surface brightness profile fitting for our samples at $z \sim 7-12$, using GALFIT and making use of our simulation results to correct for any systematic effects. We analyze each of the objects with $> 15\sigma$ detections individually (9 z_{850}-dropouts, 6 Y_{105}-dropouts), as well as the $z = 11.9$ object, which is formally detected at $\sim 8\sigma$. We extend the analysis to fainter magnitudes using stacked observations. The fainter z_{850}- and Y_{105}-dropouts are split into two luminosity bins before stacking ($0.12 < L/L^*_{z=3} < 0.3$ and $0.048 < L/L^*_{z=3} < 0.12$), whereas we group all $z \sim 9$ candidates into a single stack.

Figure 4 presents the results of Sérsic profile fitting for the 9 bright z_{850}-dropouts. Shown, from left to right, are the $3'' \times 3''$ cut-outs of the original image, the best-fit model produced by GALFIT, the residual images (original image − best-fit profile) and the segmentation maps used for masking all the neighboring objects during the profile fitting. Figure 5 similarly shows the results for the 6 bright Y_{105}-dropouts. All the objects are cleanly subtracted in the residual images. Note, however that three of the objects; two of the brightest z_{850}-dropouts, UDF12-4258-6567 and UDF12-3746-6327, as well as one of the Y_{105}-dropouts, UDF12-3952-7173 are significantly blended with neighboring objects in the original images. In addition, one of the Y_{105}-dropouts, UDF12-4470-6442 shows two cores. The uncertainties in the derived profile parameters for these objects will therefore be larger than for other isolated objects.

Figure 6 shows the profile fitting result for the $z \sim 12$ object, UDF12-3954-6284. Since the magnitude of the $z \sim 12$ object in H_{160} measured with $0.50''$-diameter aperture is 29.2 mag, corresponding to S/N $\sim$ 8, the profile fitting for this object is quite challenging. Actually, the best-fit model galaxy profile seems more elongated than that in the original image shown in Figure 6, which would overestimate of its total magnitude. At least, the residual image in Figure 6 does not clearly show any noticeable residuals around the central position, although the uncertainties of the fitting parameters are relatively large as inferred from the moderate S/N ratio. If we measure the curve of growth for this object, using progressively larger circular apertures, we find that the magnitude saturates at 28.8 mag within an aperture diameter $\sim 0.45''$. We also find by this robust method that the half-light of the source is covered by about $0.35''$-diameter aperture, and after considering the PSF broadening effect, we obtain its half-light radius, $r_{\rm hl} = 0.45$ kpc, which is consistent with the GALFIT measurement within $\sim 1\sigma$, and is also nearly equal to

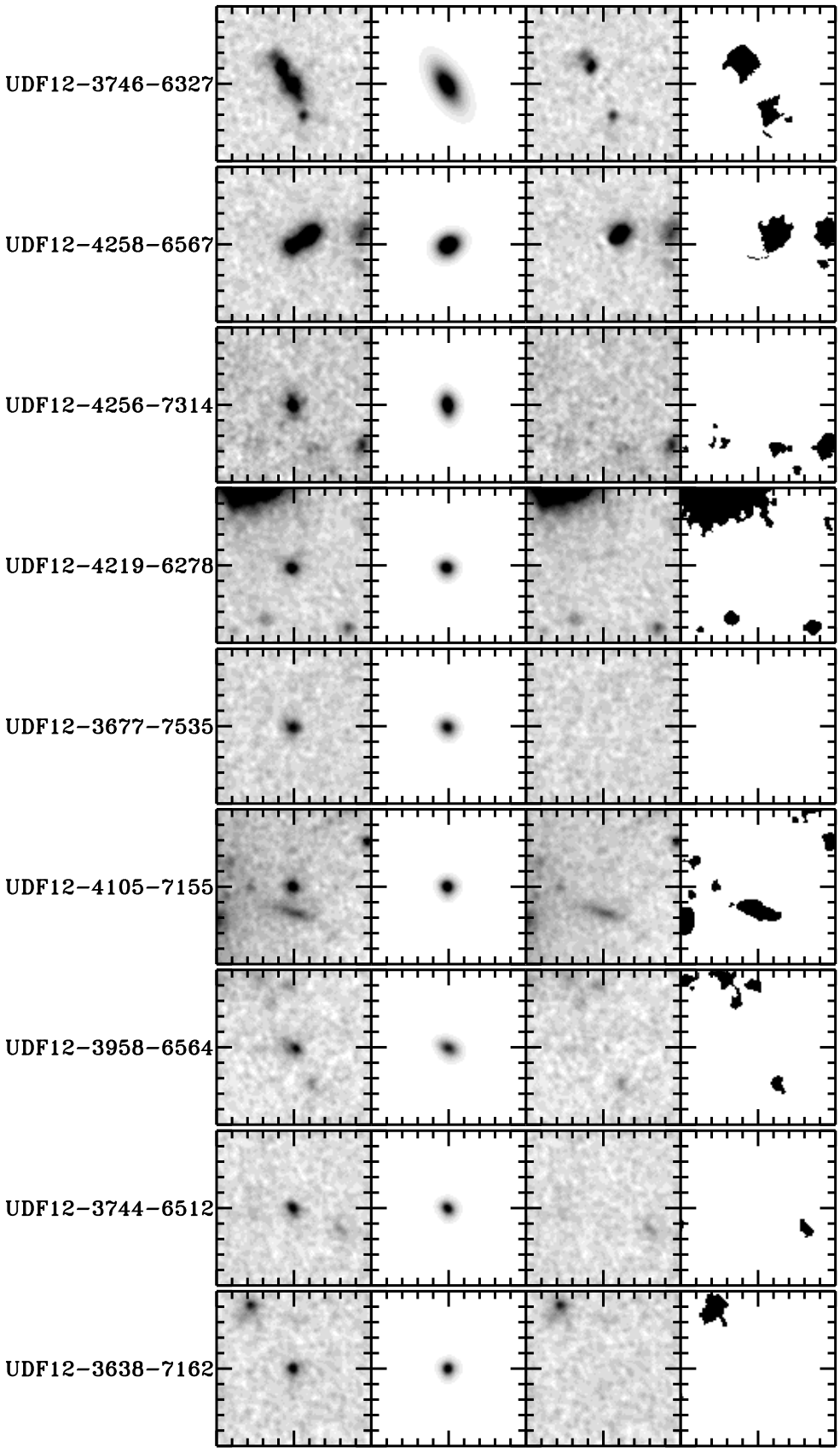

Figure 4. Sérsic profile fitting results for bright z_{850}-dropouts found in the HUDF main field. Shown, from left to right, are the $3'' \times 3''$ cut-outs of the original image, the best-fit model profile images, the residual images which are made by subtracting the best-fit images from the original ones, and the segmentation maps used for masking all the neighboring objects during the profile fitting.

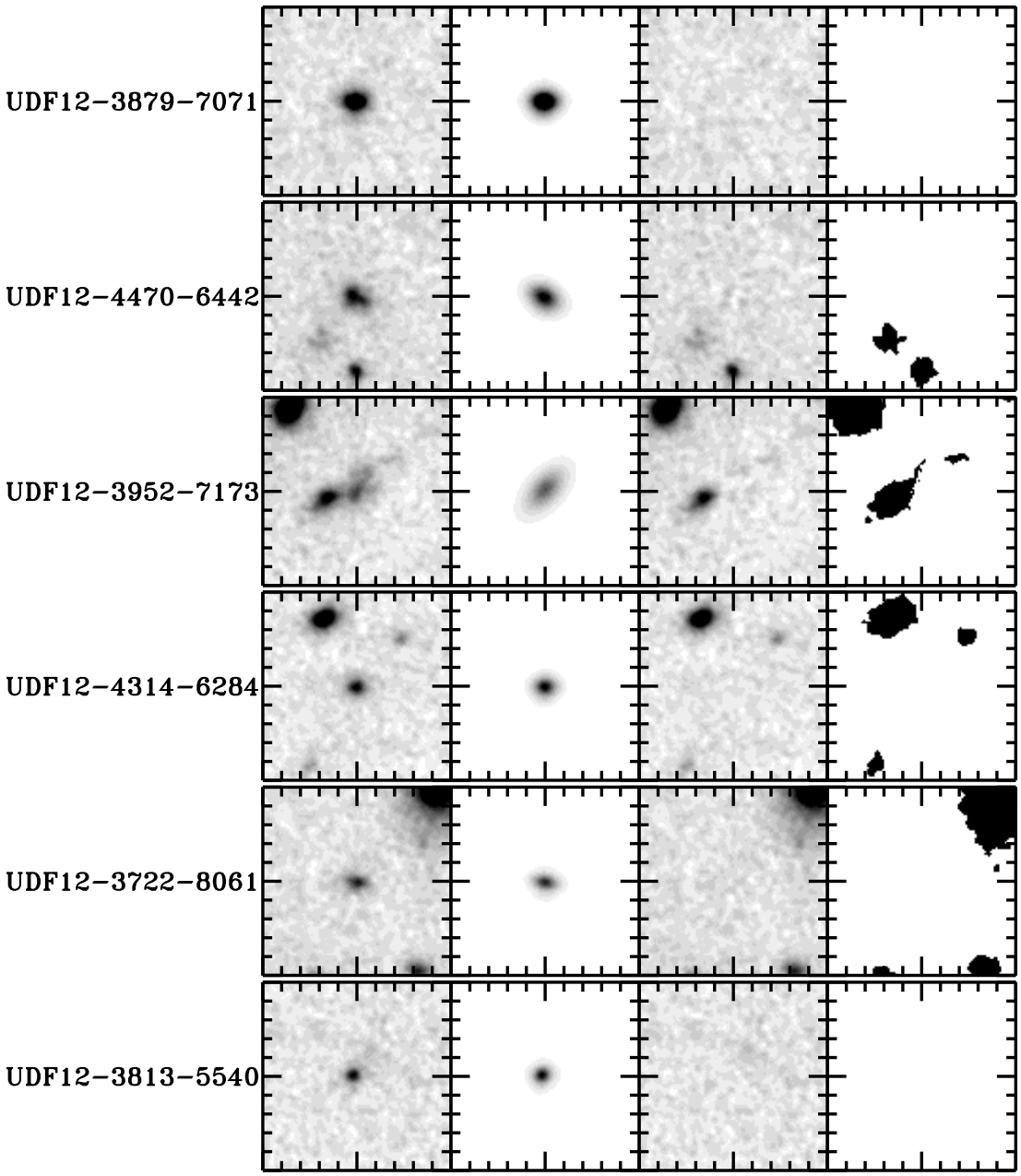

Figure 5. Sérsic profile fitting results for bright Y_{105}-dropouts found in the HUDF main field. Shown, from left to right, are the $3'' \times 3''$ cut-outs of the original image, the best-fit model profile images, the residual images which are made by subtracting the best-fit images from the original ones, and the segmentation maps used for masking all the neighboring objects during the profile fitting.

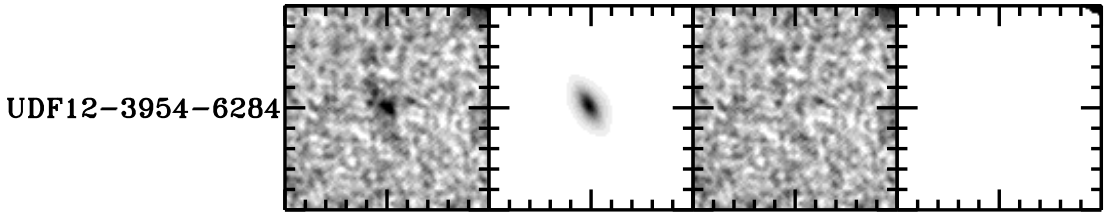

Figure 6. Sérsic profile fitting results for the $z \sim 12$ source, UDF12-3954-6284. Shown, from left to right, are the $3'' \times 3''$ cut-outs of the original image, the best-fit model profile images, the residual images which are made by subtracting the best-fit images from the original ones, and the segmentation maps used for masking all the neighboring objects during the profile fitting.

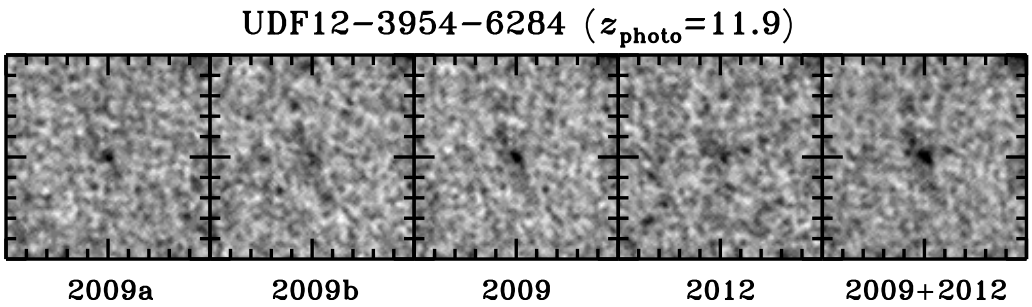

Figure 7. $3'' \times 3''$ cut-outs of the $z \sim 12$ source UDF12-3954-6284 from various subsets of the WFC3/IR H_{160}-band observations. From left to right, the first half of the 2009 dataset, the second half of the 2009 dataset, the full 53-orbit 2009 dataset, the 26-orbit 2012, and the full 84-orbit dataset (including 2009, 2012, and other exposures in this field).

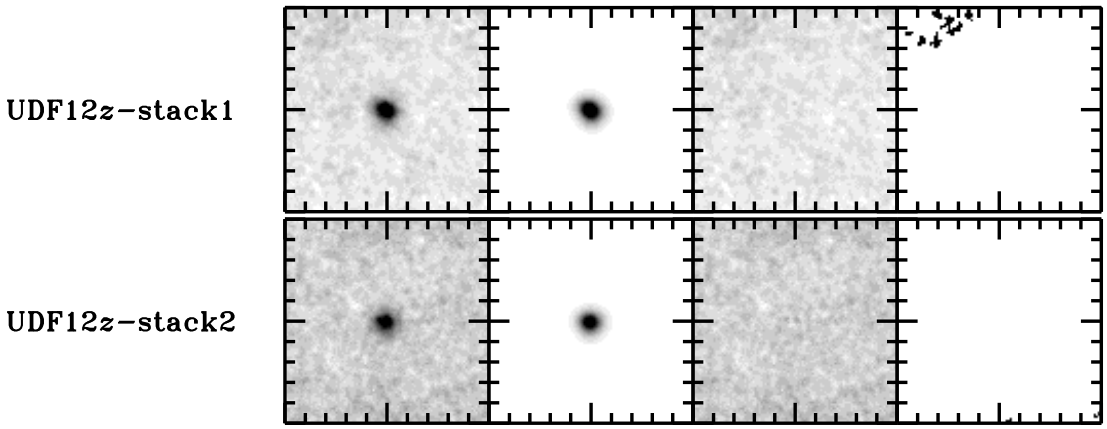

Figure 8. Same as Figure 4, except that the objects are the stacked z_{850}-dropouts, whose UV luminosities are $L = (0.12-0.3)L^*_{z=3}$ (top) and $L = (0.048-0.12)L^*_{z=3}$ (bottom).

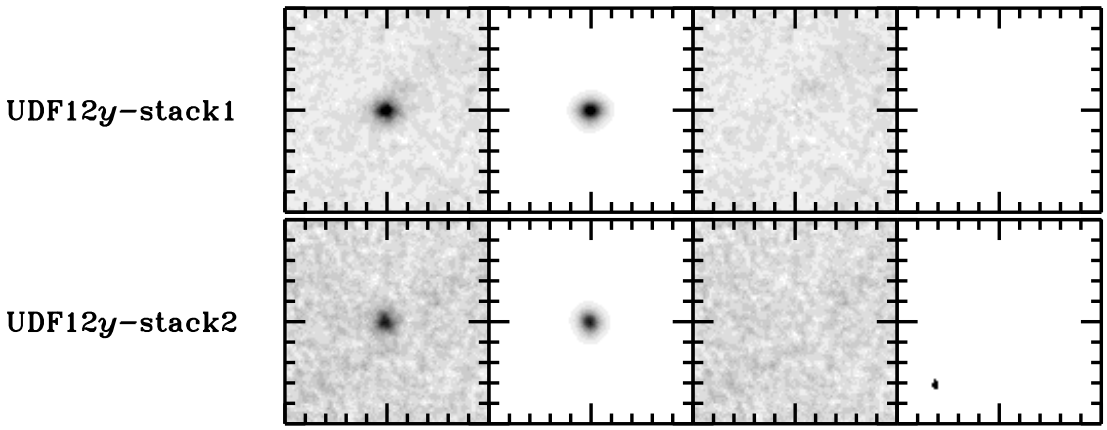

Figure 9. Same as Figure 8, except that the objects are the stacked Y_{105}-dropouts.

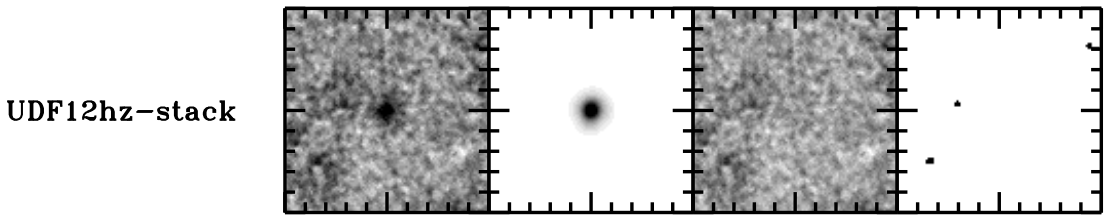

Figure 10. Same as Figure 8, except that the object is the stacked $z \sim 9$ object.

the value reported by Bouwens et al. (2012a), ~ 0.5 kpc.

Additionally, we note that this object has an unusual morphology. It is visually confirmed that the $z \sim 12$ object has a diffuse filamentary structure stretching from north-east to south-west, although the significance is very low. This has been already mentioned very recently by Bouwens et al. (2012a). Figure 7 shows the cutout H_{160} images of this object from various subsets and the full data. The diffuse structure is seen in the full (2009+2012) data and in the 2009 data. The 2009b cutout also shows a low-S/N filament, and the 2009a cutout has a similar pattern along the same direction. If this diffuse filament is indeed associated with the source at $z \sim 12$, it corresponds to its bright UV continuum and/or Lyα, which would suggest that this object is experiencing a major merger event, leading to their high star-formation activity. This star formation enhancement may explain the visibility of such a high-redshift galaxy.

Figure 8 and 9 show profile fitting results for the stacked z_{850}-dropouts and Y_{105}-dropouts, respectively, whose UV luminosities are $L = (0.12-0.3)L^*_{z=3}$ (top) and $L = (0.048-0.12)L^*_{z=3}$ (bottom). Also shown in Figure 10 is the profile fitting result for the stacked $z \simeq 9$ candidates. Note that we also make averaged (not median-stacked) images and perform profile fitting using `GALFIT`, which yield similar fitting results, although for some of the average stacks, `GALFIT` does not provide a reasonable fit due to severe confusion with neighboring objects.

In the brightest luminosity bin, $L = (0.3-1)L^*_{z=3}$, we do not perform a stacking analysis, since the numbers of the dropouts are small (2 for z_{850}-dropouts and 3 for Y_{105}-dropouts) and the stacked images are significantly confused by neighboring objects. Instead, we calculate their average sizes and magnitudes; $r_e = 0.79 \pm 0.29$ kpc and $M_{\rm UV} = -20.33 \pm 0.20$ mag ($z \sim 7$) and $r_e = 0.67 \pm 0.28$ kpc and $M_{\rm UV} = -20.08 \pm 0.10$ mag ($z \sim 8$).

The best-fit parameters are summarized in Table 3 for the z_{850}-dropouts, Table 4 for the Y_{105}-dropouts, and Table 5 for the $z > 8.5$ candidates. The weighted mean of half-light radii for the z_{850}-dropouts and Y_{105}-dropouts with $L = (0.05-1)L^*_{z=3}$ are 0.35 ± 0.07 kpc and 0.38 ± 0.09 kpc, respectively. In the next section, we present the size-luminosity relation, and investigate the redshift evolution of galaxy sizes and SFR surface densities based on these results.

5. RESULTS AND DISCUSSION

Our measurements of half-light radii in Tables 3−5 show very small values, typically $\lesssim 0.5$ kpc (see also filled symbols in Figure 11). The average half-light radii of the dropouts are only $\simeq 0.3-0.4$ kpc at $z \sim 7-8$ (Section 4.2) and at $z > 8.5$ (Table 5). The half-light radius of our $z \sim 12$ candidate is also remarkably small, 0.32 ± 0.14 kpc. Even including the 1σ uncertainties, these half-light radii are, coincidentally, just as large as those of giant molecular associations (GMAs) with a mass of $\sim 10^7 M_\odot$ found in the local universe (e.g., Vogel et al. 1988; Rand & Kulkarni 1990; Tosaki et al. 2007).

We investigate the relation between size and luminosity, i.e. the size-luminosity relation, at each redshift. Figure 11 presents the size-luminosity relation for our

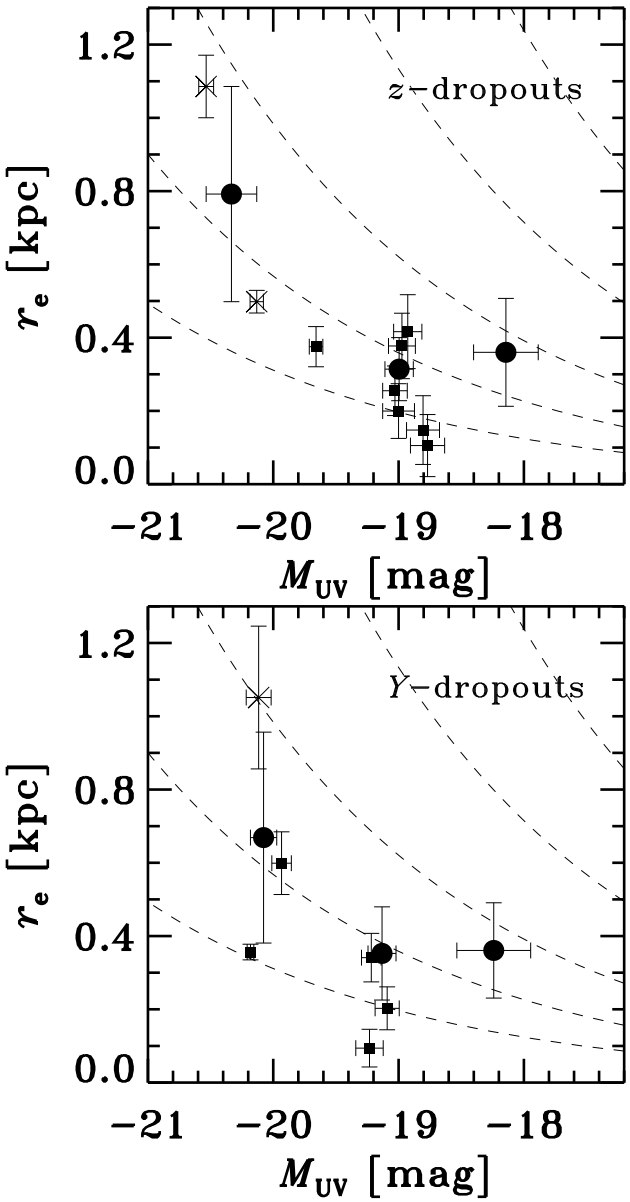

Figure 11. The size-luminosity relation for z_{850}-dropouts (top) and Y_{105}-dropouts bottom. The filled circles correspond to the stacked objects with UV luminosities of $L = (0.12-0.3)L^*_{z=3}$, $L = (0.048-0.12)L^*_{z=3}$, and the averaged values of the objects with $L = (0.3-1)L^*_{z=3}$. The filled squares show the bright objects detected at $> 15\sigma$ without any blending with neighboring sources, while the crosses show the objects detected in more than 15σ and blended with a neighboring source. The dashed curves in each figure correspond to a constant star-formation rate density $\Sigma_{\rm SFR}$ $[M_\odot\ {\rm yr}^{-1}\ {\rm kpc}^{-2}] = 0.1$, 0.3, 1, 3, 10 from top to bottom.

z_{850}-dropout and Y_{105}-dropout galaxies at $z \sim 7-8$. Our $z > 8.5$ galaxy candidates are not shown, because we cannot constrain the relation with only two measurements (one from an individual object and one from the stack). In Figure 11, fainter galaxies have a smaller half-light radius than brighter galaxies. This trend is the same as those of local galaxies (de Jong & Lacey 2000) as well as high-z dropout galaxies at slightly lower redshifts ($z \sim 6-7$), studied by Grazian et al. (2012). Because the luminosity of a galaxy depends on two physical quantities (surface brightness and size), one needs to clarify which quantity is dominant in shaping the size-

Table 3
Surface Brightness Profile Fitting Results for Bright z_{850}-dropouts

Object ID	RA†1 [h:m:s]	Decl.†1 [d:m:s]	$m_{\rm UV}^{\rm (ap)}$†2 [mag]	n†3	$m_{\rm UV}$†4 [mag]	$M_{\rm UV}$†5 [mag]	r_e†6 [kpc]
S/N> 15, $L/L^*_{z=3} = 0.3-1$							
UDF12-3746-6327	3:32:37.46	−27:46:32.7	27.38	1.0	26.25 ± 0.06	-20.54 ± 0.06	1.09 ± 0.09
UDF12-4258-6567	3:32:42.58	−27:46:56.7	27.41	1.0	26.74 ± 0.05	-20.13 ± 0.05	0.50 ± 0.03
S/N> 15, $L/L^*_{z=3} = 0.12-0.3$							
UDF12-4256-7314	3:32:42.56	−27:47:31.4	27.73	1.0	27.23 ± 0.05	-19.66 ± 0.05	0.38 ± 0.05
UDF12-4219-6278	3:32:42.19	−27:46:27.8	28.09	1.0	27.74 ± 0.10	-19.03 ± 0.10	0.26 ± 0.07
UDF12-3677-7535	3:32:36.77	−27:47:53.5	28.22	1.0	27.82 ± 0.11	-18.97 ± 0.11	0.38 ± 0.09
UDF12-4105-7155	3:32:41.05	−27:47:15.5	28.30	1.0	27.98 ± 0.13	-19.00 ± 0.13	0.20 ± 0.07
UDF12-3958-6564	3:32:39.58	−27:46:56.4	28.33	1.0	27.87 ± 0.11	-18.93 ± 0.11	0.42 ± 0.10
UDF12-3744-6512	3:32:37.44	−27:46:51.2	28.38	1.0	28.02 ± 0.13	-18.80 ± 0.13	0.15 ± 0.09
UDF12-3638-7162	3:32:36.38	−27:47:16.2	28.41	1.0	28.05 ± 0.14	-18.77 ± 0.14	0.11 ± 0.08
stack							
UDF12z-stack1 ($L/L^*_{z=3} = 0.12-0.3$)			28.27	1.0	27.87 ± 0.11	-19.00 ± 0.11	0.31 ± 0.09
UDF12z-stack2 ($L/L^*_{z=3} = 0.048-0.12$)			29.20	1.0	28.73 ± 0.26	-18.14 ± 0.26	0.36 ± 0.15

†1 Coordinates are in J2000.
†2 Measured in 0.46″-diameter aperture with the stack of the J_{125} and J_{140} images.
†3 Sérsic index. This is fixed, not measured.
†4 Total magnitude measured by `GALFIT`. The systematic effect is considered.
†5 Total absolute magnitude calculated using $z_{\rm photo}$ if available, otherwise $z = 6.7$, which corresponds to the peak of the selection function for z_{850}-dropouts.
†6 Circularized half-light radius $r_e = a\sqrt{b/a}$, where a is radius along the major axis, and b/a is axis ratio.

Table 4
Surface Brightness Profile Fitting Results for Bright Y_{105}-dropouts

Object ID	RA†1 [h:m:s]	Decl.†1 [d:m:s]	$m_{\rm UV}^{\rm (ap)}$†2 [mag]	n†3	$m_{\rm UV}$†4 [mag]	$M_{\rm UV}$†5 [mag]	r_e†6 [kpc]
S/N> 15, $L/L^*_{z=3} = 0.3-1$							
UDF12-3879-7071	3:32:38.80	−27:47:07.1	27.21	1.0	26.80 ± 0.03	-20.18 ± 0.03	0.36 ± 0.02
UDF12-4470-6442	3:32:44.70	−27:46:44.2	27.69	1.0	27.13 ± 0.08	-19.93 ± 0.08	0.60 ± 0.09
UDF12-3952-7173	3:32:39.52	−27:47:17.3	28.10	1.0	26.95 ± 0.10	-20.12 ± 0.10	1.05 ± 0.19
S/N> 15, $L/L^*_{z=3} = 0.12-0.3$							
UDF12-4314-6284	3:32:43.14	−27:46:28.4	28.10	1.0	27.73 ± 0.08	-19.22 ± 0.08	0.34 ± 0.07
UDF12-3722-8061	3:32:37.22	−27:48:06.1	28.28	1.0	27.89 ± 0.10	-19.09 ± 0.10	0.20 ± 0.06
UDF12-3813-5540	3:32:38.13	−27:45:54.0	28.33	1.0	27.99 ± 0.11	-19.23 ± 0.11	0.09 ± 0.05
stack							
UDF12y-stack1 ($L/L^*_{z=3} = 0.12-0.3$)			28.40	1.0	28.01 ± 0.11	-19.13 ± 0.11	0.35 ± 0.13
UDF12y-stack2 ($L/L^*_{z=3} = 0.048-0.12$)			29.47	1.0	28.90 ± 0.29	-18.24 ± 0.29	0.36 ± 0.13

†1 Coordinates are in J2000.
†2 Measured in 0.50″-diameter aperture with the stack of the J_{140} and H_{160} images.
†3 Sérsic index. This is fixed, not measured.
†4 Total magnitude measured by `GALFIT`. The systematic effect is considered.
†5 Total absolute magnitude calculated using $z_{\rm photo}$ if available, otherwise $z = 8.0$, which corresponds to the peak of the selection function for Y_{105}-dropouts.
†6 Circularized half-light radius $r_e = a\sqrt{b/a}$, where a is radius along the major axis, and b/a is axis ratio.

luminosity relation. We define star-formation rate surface density, $\Sigma_{\rm SFR}$, as the average star-formation rate in a circle whose radius is r_e,

$$\Sigma_{\rm SFR}\,[M_\odot\,{\rm yr}^{-1}\,{\rm kpc}^{-2}] \equiv \frac{{\rm SFR}/2}{\pi r_e^2}. \quad (2)$$

In the case that dust extinction is negligible, a rest-frame UV luminosity density approximately correlates with a star-formation rate (Kennicutt 1998a),

$${\rm SFR}\,[M_\odot\,{\rm yr}^{-1}] = 1.4\times10^{-28} L_\nu\,[{\rm erg\,s^{-1}Hz^{-1}}]. \quad (3)$$

From equations (2)−(3), we obtain

$$M_{\rm UV} = -2.5\log\left(\frac{\Sigma_{\rm SFR}\,r_e^2}{1.4\times10^{-28}\cdot 2\cdot(10{\rm pc}\,[{\rm cm}])^2}\right) - 48.6. \quad (4)$$

In Figure 11, we show constant star-formation rate surface densities of $\Sigma_{\rm SFR} = 0.1$, 0.3, 1, 3, and 10 [$M_\odot$ yr^{-1} kpc^{-2}] with dashed lines. We find that most of individual galaxies and stacked galaxies fall in the range of $\Sigma_{\rm SFR} \simeq 1-10$ within their uncertainties. These results indicate that both bright and faint $z \sim 7-8$ galaxies have similar star-formation rate surface densities of $\Sigma_{\rm SFR} \simeq 1-10$, and that the size-luminosity relation at each redshift is mainly determined by the size of galaxies

Table 5
Surface Brightness Profile Fitting Results for $z > 8.5$ Candidates

Object ID	RA†1 [h:m:s]	Decl.†1 [d:m:s]	$m_{\rm UV}^{\rm (ap)}$†2 [mag]	n†3	$m_{\rm UV}$†4 [mag]	$M_{\rm UV}$†5 [mag]	r_e†6 [kpc]
UDF12-3954-6284	3:32:39.54	−27:46:28.4	29.24	1.0	28.47 ± 0.25	-20.41 ± 0.25	0.32 ± 0.14
stack							
UDF12hz-stack			29.69	1.0	29.11 ± 0.49	-18.21 ± 0.49	0.35 ± 0.16

†1 Coordinates are in J2000.
†2 Measured in 0.50″-diameter aperture with the H_{160} image.
†3 Sérsic index. This is fixed, not measured.
†4 Total magnitude measured by GALFIT. The systematic effect is considered. For UDF12-3954-6284, this might be overestimated, since the best-fit model galaxy profile seems more elongated than that in the original image shown in Figure 6. If we measure the curve of growth for this source, the magnitude saturates at 28.8 mag (See Section 4.2).
†5 Total absolute magnitude. We calculate it with $z_{\rm photo} = 11.9$ for UDF12-3954-6284, considering IGM absorption shortward of its Lyα wavelength. We use the average photometric redshift, $z_{\rm photo} = 9.0$ for the stacked object.
†6 Circularized half-light radius $r_e = a\sqrt{b/a}$, where a is radius along the major axis, and b/a is axis ratio.

that have a similar star-formation rate surface density.

We then investigate the size evolution. Since the half-light radius depends on luminosity, as displayed by the size-luminosity relation, we carefully compare the half-light radii of our dropout galaxies within a fixed magnitude range. Figure 12 presents the average half-light radius as a function of redshift for our dropout galaxies at $z \sim 7-12$ with $(0.3-1)L^*_{z=3}$ and $(0.12-0.3)L^*_{z=3}$, together with dropout galaxies at $z \sim 4-8$ taken from the literature. Our measurements of average half-light radii are consistent with those from the previous studies at $z \sim 7-8$, where we see overlap with previous measurements. Figure 12 indicates that the average half-light radius decreases with redshift from $z \sim 4$ to 8, which is consistent with the claims of previous studies (e.g. Ferguson et al. 2004; Bouwens et al. 2004; Hathi et al. 2008; Oesch et al. 2010a).

UDF12 provides us with the deepest ever near-infrared images of the HUDF, allowing our study to extend the dynamic range of redshift in the size evolution analysis from $z \sim 8$ to $z \sim 12$, and identifies that the decreasing trend holds up to $z \sim 12$ as shown in Figure 12, if the putative $z \sim 12$ source is real. Although the statistical uncertainty of measurement is large, the half-light radius of $z \sim 12$ is $r_e = 0.32 \pm 0.14$ kpc in the luminosity bin of $(0.3-1)L^*_{z=3}$, which is significantly smaller than that of $z \sim 6$ by a factor of 3. Note that we can only plot the half-light radius at $z \sim 12$ on the panel of $(0.3-1)L^*_{z=3}$ in Figure 12, because there are no $z \sim 12$ galaxies with $(0.12-0.3)L^*_{z=3}$ in the UDF12 data. Similarly, our stack of $z > 8.5$ galaxies have a luminosity fainter than $(0.12-0.3)L^*_{z=3}$, which is too faint to be compared with the baseline of the average half-light radii at $z \sim 4-6$. However, our results of $z > 7$ galaxies at these faint magnitudes, which are shown as gray filled circles in the bottom panel of Figure 12, are consistent with the decreasing trend of the half-light radius, albeit with large errors.

This decreasing trend may be explained by the evolution of host dark halo radius. According to the analytic model in the hierarchical structure formation framework of ΛCDM (see, e.g., Mo et al. 1998; Mo & White 2002; Ferguson et al. 2004), the virial radius of a dark matter halo is given by

$$r_{\rm vir} = \left(\frac{GM_{\rm vir}}{100H(z)^2} \right)^{1/3}, \quad (5)$$

where $H(z)$ is the Hubble parameter and $M_{\rm vir}$ is the virial mass of the halo. The virial radius is also expressed as a function of the circular velocity of dark halo by

$$r_{\rm vir} = \frac{v_{\rm vir}}{10H(z)}. \quad (6)$$

Since $H(z)$ is approximated by $\sim (1+z)^{3/2}$ in a flat universe at high redshifts, the redshift evolution of the virial radius is $r_{\rm vir} \propto H(z)^{-2/3} \sim (1+z)^{-1}$ for constant halo mass and $r_{\rm vir} \propto H(z)^{-1} \sim (1+z)^{-1.5}$ for constant velocity.

Figure 12 shows the radius-redshift relation of dark matter halos for the case of constant halo mass and constant velocity. Previous studies investigating the radius-redshift relation in the redshift range $4 < z < 8$ reach two different conclusions. Bouwens et al. (2004, 2006) claim that the relation is roughly $(1+z)^{-1}$, suggestive that the sizes of disks scale with constant halo mass, while Ferguson et al. (2004) and Hathi et al. (2008) argue that $(1+z)^{-1.5}$, i.e., the constant velocity case, is preferable. We fit the radius-redshift relation over a wider range of redshift (extending to $z \sim 12$) with a function of $(1+z)^s$, where s is a free parameter. We take into account our size measurements: for the brighter bin, the average sizes of z_{850}- and Y_{105}-dropouts and the size of the $z \sim 12$ source, and for the fainter bin, the measured sizes of the stacks of z_{850}- and Y_{105}-dropouts with $L = (0.12-0.3)L^*_{z=3}$. In addition, we use the results reported in the literature: the average sizes at $z = 2.5$ (Bouwens et al. 2004), the average sizes at $z = 4-6$ (Oesch et al. 2010a)[17]. We fit the following two functions to the data, $\log r_e = s\log(1+z) + a_1$ for $L = (0.3-1)L^*_{z=3}$ and $\log r_e = s\log(1+z) + a_2$ for $L = (0.12-0.3)L^*_{z=3}$, where s, a_1, and a_2 are free parameters. Varying the three parameters, we search for the

[17] For the fitting, we do not utilize the GALFIT measurements by Oesch et al. (2010a), which they did not use as their fiducial ones. Note that the fitting result is consistent within 1σ, if we include the GALFIT measurements instead of their SExtractor measurements.

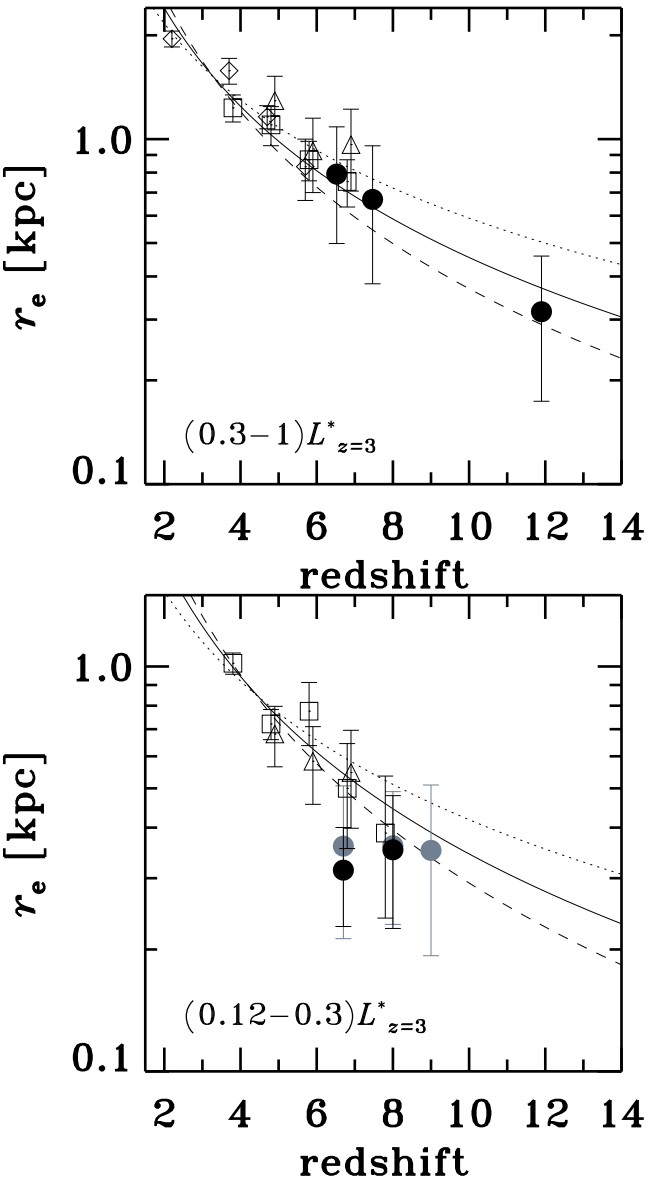

Figure 12. **Top**: Evolution of the half-light radius across the redshift range from $z \sim 2$ to 12 in $(0.3-1)L^*_{z=3}$. The filled circles show the average sizes of our z_{850}-dropouts and Y_{105}-dropouts, and the size of the $z \sim 12$ object. The open symbols are taken from the literature; the open squares and triangles are dropout galaxies taken from Oesch et al. (2010a), the open diamonds are from Bouwens et al. (2004). After excluding the sample overlaps, we fit simple functions of $(1+z)^s$ with the data in both luminosity bins, and obtain $s = -1.28 \pm 0.13$. which is shown as the solid line. The dotted and dashed lines correspond to the case of $s = -1.0$ and -1.5, respectively. **Bottom**: Evolution of the half-light radius across the redshift range from $z \sim 4$ to 8 in $(0.12-0.3)L^*_{z=3}$. The open and filled black symbols denote the same as those in the top panel. The gray filled circles are dropout galaxies in the fainter luminosity bin, $(0.048-0.12)L^*_{z=3}$. The solid, dotted, and dashed lines are the same as those in the top figure.

best-fitting set of (s, a_1, a_2) that minimizes χ^2. The best-fit parameters are $s = -1.28 \pm 0.13$, $a_1 = 0.99 \pm 0.08$, and $a_2 = 0.87^{+0.09}_{-0.10}$. We have checked that exclusion of the the putative $z \simeq 12$ object produces no significant change in our results, but it is nevertheless interesting that its size conforms with the trend established at slightly lower redshifts. We note that these results are clearly consistent with the redshift trend derived by Oesch et al. (2010a) from the early UDF09 data, as they reported $s = -1.12 \pm 0.17$ for galaxies with luminosities in the range $L = (0.3-1)L^*_{z=3}$, and $s = -1.32 \pm 0.52$ for the fainter galaxies with $L = (0.12-0.3)L^*_{z=3}$. However, our derived value for s is more accurate, both because of the improved data and galaxy samples provided by UDF12, and because we have chosen to fit a single value of s to both the bright and more modest luminosity galaxies.

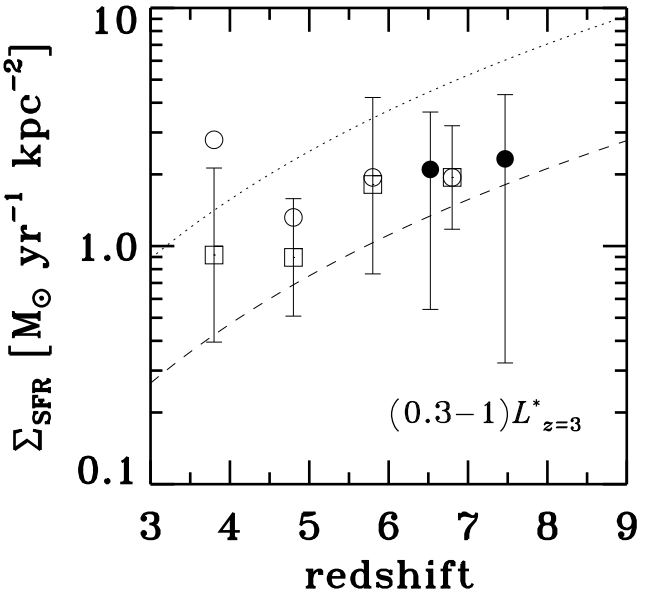

Figure 13. Evolution of the SFR surface density $\Sigma_{\rm SFR}$ as a function of redshift, for dropouts in the brightest luminosity bin, $L = (0.3-1)L^*_{z=3}$. The filled circles correspond to our z_{850}-dropouts and Y_{105}-dropouts. The open squares are taken from Oesch et al. (2010a), showing their dropout galaxies, while the open circles are the same objects but corrected for dust absorption. The dotted line and dashed line shows the case with a constant UV luminosity $L = L^*_{z=3}$ and $0.3L^*_{z=3}$, respectively, given that their half-light radii follow the simple relation of $(1+z)^s$, which is derived in Section 5 and shown in Figure 12.

It should be noted again that the above simple constant mass or content velocity models assume that the stellar to halo size ratio does not change over this redshift range (Mo et al. 1998). To properly interpret our result, more realistic models are needed which carefully treat the stellar to halo size ratio, as well as consider effects on galaxy sizes from galaxy mergers, torquing, and feedback, based on a hierarchical galaxy formation scenario over the full redshift range (e.g., Somerville et al. 2008). These size measurements of high-redshift galaxies provide a launching point for a theoretical understanding of the structure of such galaxies, which has only recently been attempted but is of critical importance in understanding their properties (e.g., Muñoz & Furlanetto 2012).

Figure 13 presents the average star-formation surface density, $\Sigma_{\rm SFR}$, as a function of redshift. Note that the measurements are shown up to $z \sim 8$ in Figure 13, because the uncertainty of the $z \sim 12$ measurements are too large to place a meaningful constraint. Our galaxies at $z > 7$ have $\Sigma_{\rm SFR} \sim 2$. $\Sigma_{\rm SFR}$ appears to increase towards high redshifts. In fact, this increase of $\Sigma_{\rm SFR}$ is expected from the decreasing trend of galaxy size at a given luminosity (Figure 12). Since $\Sigma_{\rm SFR}$ is proportional to the UV luminosity density in the case of no dust extinction, Figure 13 indicates that UV luminosity surface brightness is higher for $z \sim 7-8$ galaxies than for

$z \sim 4-5$ galaxies by a factor of $2-3$. Figure 13 has data points of dust-corrected $\Sigma_{\rm SFR}$. The dust-extinction corrected $\Sigma_{\rm SFR}$ is significantly larger than uncorrected $\Sigma_{\rm SFR}$ at $z \sim 4-5$, while almost no difference is found at $z > 6$. Oesch et al. (2010a) claim that the dust-extinction corrected $\Sigma_{\rm SFR}$ is roughly constant over the redshift range of $z \sim 3-7$. Extending their study, we find this constant $\Sigma_{\rm SFR}$ up to $z \sim 8$. Dotted and dashed lines in Figure 13 show the $\Sigma_{\rm SFR}$ values for $L^*_{z=3}$ and $0.3L^*_{z=3}$ expected from the best-fit size evolution of $(1+z)^s$. These lines imply that one would find galaxies with extremely high $\Sigma_{\rm SFR}$ at $z \gtrsim 10$ and beyond. A simple increase of the average $\Sigma_{\rm SFR}$ is not expected, however. This is because the typical UV luminosity, L^*, is fainter at higher redshifts and galaxies with $(0.3-1.0)L^*_{z=3}$ are quite rare at $z \gtrsim 10$. In this sense, even higher-redshift galaxies cannot take an extremely high average $\Sigma_{\rm SFR}$ beyond $\sim 3-10\ M_\odot\ {\rm yr}^{-1}\ {\rm kpc}^{-2}$. In the local universe, the SFR surface densities of normal disk galaxies are about $0.01 M_\odot\ {\rm yr}^{-1}\ {\rm kpc}^{-2}$, smaller than what we have found for $z \sim 4-8$ dropouts. The centers of normal disk galaxies, on the other hand, reach about $1 M_\odot\ {\rm yr}^{-1}\ {\rm kpc}^{-2}$ (Kennicutt 1998b, see also Momose et al. 2010), which is comparable to $\Sigma_{\rm SFR}$ of $z \sim 4-8$ dropouts. Because local starbursts, especially nuclear starbursts, have high $\Sigma_{\rm SFR}$ up to $100-1000 M_\odot\ {\rm yr}^{-1}\ {\rm kpc}^{-2}$ (Kennicutt 1998b), the star-formation surface density of dropout galaxies at $z \sim 4-8$ is significantly smaller than those of the extreme population found in the local universe, which indicate that star-formation in dropout galaxies is not as rapid as that of local extreme starbursts. Speculatively, because high-z dropouts are metal and dust poor galaxies (e.g., Bouwens et al. 2012b), gas cooling in a given amount of molecular clouds of high-z dropouts would be less efficient than that of local starbursts.

6. SUMMARY

In this paper, we have presented sizes of dropout galaxy candidates at $z \sim 7-12$ identified by the 2012 Hubble Ultra Deep Field campaign. We have stacked the new F140W image with the existing F125W image and the deeper F160W image, to maximize the available depth at rest-frame wavelengths $\lambda_{\rm rest} \simeq 1600-1700$Å for z_{850}-dropout and Y_{105}-dropout samples respectively, allowing secure size measurement from $> 15\sigma$ detections. The extremely deep F105W data ensures that $z > 8$ candidates are robust, extending the redshift range of reliable objects. We have performed surface brightness profile fitting for our samples at $z \sim 7-12$. Our measurements have shown that the average half-light radii of galaxies are very small, $0.3-0.4$ kpc at $z \sim 7-12$. Such sizes are, perhaps coincidentally, comparable to the sizes of giant molecular associations in local star-forming galaxies.

Combining our new results at $z \simeq 7-12$ with existing average size measurements previously reported for dropout galaxies at $z \simeq 4-7$, we have investigated the size evolution of dropout galaxies. We have confirmed the trend for size to decrease with increasing redshift (at a given luminosity) and have shown that this trend appears to extend out to $z \simeq 12$. Motivated by the fact that, at least qualitatively, the sizes of the brighter $(0.3-1.0L^*_{z=3})$ and somewhat fainter $(0.12-0.3L^*_{z=3})$ dropout galaxies show a similar trend with redshift, we have attempted to model the size evolution of both samples together with a function of the form $(1+z)^s$ over the redshift range $z \simeq 4-12$. The result is a best-fitting parameter value of $s = -1.28 \pm 0.13$, approximately mid-way between the physically expected evolution for baryons embedded in dark halos of constant mass ($s = -1$) and constant velocity ($s = -1.5$). This evolution is consistent with that derived by Oesch et al. (2010a), albeit our derived evolution with redshift is slightly steeper than that derived by Oesch et al. (2010a) for the brighter galaxies. We have checked that our best-fitting value of s is not significantly affected if the putative $z \simeq 12$ galaxy is excluded, but it is interesting that this object has a half-light radius which is perfectly consistent with our best-fitting relation.

We have also found that a clear size-luminosity relation, such as that found at lower redshift, is also evident in both our z_{850}- and Y_{105}-dropout samples. This relation can be interpreted in terms of a constant surface density of star formation over a range in luminosity of $0.05-1.0L^*_{z=3}$. These size-redshift and size-luminosity relations suggest that galaxy sizes at $z > 4$ are not simply decided by the evolution of the constant mass or velocity of the parent halo and/or follow in the evolution of the stellar to halo size ratio with a similar star-formation rate density.

Finally, our results also strengthen previous claims that the star-formation surface density in dropout galaxies is broadly unchanged from $z \simeq 4$ to $z \simeq 8$ at $\Sigma_{\rm SFR} \simeq 2\,{\rm M}_\odot\,{\rm yr}^{-1}\,{\rm kpc}^{-2}$. This value is $2-3$ orders of magnitude lower than that found in extreme starburst galaxies, but is very comparable to that seen today in the centers of normal disk galaxies. This provides further support for a steady smooth build-up of the stellar populations in galaxies in the young universe.

ACKNOWLEDGEMENTS

We thank Rieko Momose and Suraphong Yuma for their helpful comments. This work was supported by Japan Society for the Promotion of Science (JSPS), Grants-in-Aid for Scientific Research (KAKENHI), Grant Numbers 24840010 and 23244025, and World Premier International Research Center Initiative (WPI Initiative), MEXT, Japan. EFCL, ABR and MC acknowledge the support of the UK Science and Technology Facilities Council. US authors acknowledge financial support from the Space Telescope Science Institute under award HST-GO-12498.01-A. JSD and RAAB acknowledge the support of the European Research Council via the award of an Advanced Grant to JSD. JSD also acknowledges the support of the Royal Society through a Wolfson Research Merit Award. SC acknowledges the support of the European Commission through the Marie Curie Initial Training Network ELIXIR. This work is based on data from the *Hubble Space Telescope* which is operated by NASA through the Space Telescope Science Institute via the association of Universities for Research in Astronomy, Inc. for NASA under contract NAS5-26555.

REFERENCES

Bertin, E., & Arnouts, S. 1996, A&AS, 117, 393

Bouwens, R. J., Illingworth, G. D., Blakeslee, J. P., Broadhurst, T. J., & Franx, M. 2004, ApJ, 611, L1
Bouwens, R. J., Illingworth, G. D., Blakeslee, J. P., & Franx, M. 2006, ApJ, 653, 53
Bouwens, R. J., Illingworth, G. D., Franx, M., & Ford, H. 2008, ApJ, 686, 230
Bouwens, R. J., Illingworth, G. D., Oesch, P. A., et al. 2010, ApJ, 709, L133
Bouwens, R. J., Illingworth, G. D., Labbe, I., et al. 2011a, Nature, 469, 504
Bouwens, R. J., Illingworth, G. D., Oesch, P. A., et al. 2011b, ApJ, 737, 90
Bouwens, R. J., Oesch, P. A., Illingworth, G. D., et al. 2012a, ArXiv e-prints (arXiv:1211.3105)
Bouwens, R. J., Illingworth, G. D., Oesch, P. A., et al. 2012b, ApJ, 754, 83
Bunker, A. J., Wilkins, S., Ellis, R. S., et al. 2010, MNRAS, 409, 855
Castellano, M., Fontana, A., Boutsia, K., et al. 2010, A&A, 511, A20+
de Jong, R. S., & Lacey, C. 2000, ApJ, 545, 781
Dunlop, J. S., Rogers, A. B., McLure, R. J., et al. 2012, MNRAS, submitted (arXiv:1212.0860)
Ellis, R. S., McLure, R. J., Dunlop, J. S., et al. 2012, ApJL, accepted (arXiv:1211.6804)
Ferguson, H. C., Dickinson, M., Giavalisco, M., et al. 2004, ApJ, 600, L107
Finkelstein, S. L., Papovich, C., Giavalisco, M., et al. 2010, ApJ, 719, 1250
Fontana, A., Vanzella, E., Pentericci, L., et al. 2010, ApJ, 725, L205
Grazian, A., Castellano, M., Fontana, A., et al. 2012, A&A, 547, A51
Hathi, N. P., Malhotra, S., & Rhoads, J. E. 2008, ApJ, 673, 686
Kennicutt, Jr., R. C. 1998a, ARA&A, 36, 189
—. 1998b, ApJ, 498, 541
Koekemoer, A. M., Ellis, R. S., McLure, R. J., et al. 2012, ApJS, submitted (arXiv:1212.1448)
Lorenzoni, S., Bunker, A. J., Wilkins, S. M., et al. 2011, MNRAS, 414, 1455
McLure, R. J., Dunlop, J. S., Cirasuolo, M., et al. 2010, MNRAS, 403, 960
McLure, R. J., Dunlop, J. S., de Ravel, L., et al. 2011, MNRAS, 418, 2074
McLure, R. J., et al. 2012, in preparation
Mo, H. J., Mao, S., & White, S. D. M. 1998, MNRAS, 295, 319
—. 1999, MNRAS, 304, 175
Mo, H. J., & White, S. D. M. 2002, MNRAS, 336, 112
Momose, R., Okumura, S. K., Koda, J., & Sawada, T. 2010, ApJ, 721, 383
Mosleh, M., Williams, R. J., Franx, M., et al. 2012, ApJ, 756, L12
Muñoz, J. A., & Furlanetto, S. 2012, MNRAS, 426, 3477
Oesch, P. A., Carollo, C. M., Stiavelli, M., et al. 2009, ApJ, 690, 1350
Oesch, P. A., Bouwens, R. J., Carollo, C. M., et al. 2010a, ApJ, 709, L21
Oesch, P. A., Bouwens, R. J., Illingworth, G. D., et al. 2010b, ApJ, 709, L16
Oke, J. B., & Gunn, J. E. 1983, ApJ, 266, 713
Ouchi, M., Mobasher, B., Shimasaku, K., et al. 2009, ApJ, 706, 1136
Peng, C. Y., Ho, L. C., Impey, C. D., & Rix, H.-W. 2002, AJ, 124, 266
—. 2010, AJ, 139, 2097
Pirzkal, N., Sahu, K. C., Burgasser, A., et al. 2005, ApJ, 622, 319
Rand, R. J., & Kulkarni, S. R. 1990, ApJ, 349, L43
Robertson, B. E., et al. 2012, in preparation
Schenker, M. A., et al. 2012, in preparation
Sersic, J. L. 1968, Atlas de galaxias australes
Somerville, R. S., Barden, M., Rix, H.-W., et al. 2008, ApJ, 672, 776
Steidel, C. C., Adelberger, K. L., Giavalisco, M., Dickinson, M., & Pettini, M. 1999, ApJ, 519, 1
Tosaki, T., Shioya, Y., Kuno, N., et al. 2007, PASJ, 59, 33
Vogel, S. N., Kulkarni, S. R., & Scoville, N. Z. 1988, Nature, 334, 402
Wilkins, S. M., Bunker, A. J., Lorenzoni, S., & Caruana, J. 2011, MNRAS, 411, 23
Yan, H., Windhorst, R. A., Hathi, N. P., et al. 2010, Research in Astronomy and Astrophysics, 10, 867